Journal of Materials Chemistry A

Advanced Oxygen-Electrode-Supported Solid Oxide Electrochemical Cells with Sr(Ti,Fe)O3-δ-based Fuel Electrodes for Electricity Generation and Hydrogen Production

Journal:	*Journal of Materials Chemistry A*
Manuscript ID	TA-ART-07-2020-006678.R1
Article Type:	Paper
Date Submitted by the Author:	20-Nov-2020
Complete List of Authors:	Zhang, Shanlin; Xi'an Jiaotong University, State Key laboratory for Mechanical Behavior of Materials, School of Materials Science and Engineering Wang, Hongqian; Northwestern University, Materials Science and Engineering yang, tianrang; Northwestern University, Materials science and engineering Lu, Matthew; Northwestern University, Department of Materials Science and Engineering Li, Chengxin; Xi'an Jiaotong University, School of material Science and engineering Li, Changjiu; Xi'an Jiaotong University, School of material Science and engineering Barnett, Scott; Northwestern University, Materials Science and Engineering

Advanced Oxygen-Electrode-Supported Solid Oxide Electrochemical Cells with $Sr(Ti,Fe)O_{3-\delta}$-based Fuel Electrodes for Electricity Generation and Hydrogen Production†

Shan-Lin Zhang,[ab] Hongqian Wang,[a] Tianrang Yang,[a] Matthew Y. Lu,[a] Cheng-Xin Li,[b*] Chang-Jiu Li,[b*] and Scott A. Barnett[a*]

[a] Department of Materials Science and Engineering, Northwestern University, Evanston, Illinois 60208, USA

[b] State Key laboratory for Mechanical Behavior of Materials, School of Materials Science and Engineering, Xi'an Jiaotong University, Xi'an, Shaanxi, 710049, People's Republic of China

Abstract

$Sr(Ti_{0.3}Fe_{0.7})O_{3-\delta}$ (STF) and the associated exsolution electrodes $Sr_{0.95}(Ti_{0.3}Fe_{0.63}Ru_{0.07})O_{3-\delta}$ (STFR), or $Sr_{0.95}(Ti_{0.3}Fe_{0.63}Ni_{0.07})O_{3-\delta}$ (STFN) are alternatives to Ni-based cermet fuel electrodes for solid oxide electrochemical cells (SOCs). They can provide improved tolerance to redox cycling and fuel impurities, and may allow direct operation with hydrocarbon fuels. However, such perovskite-oxide-based electrodes present processing challenges for co-sintering with thin electrolytes to make fuel electrode supported SOCs. Thus, they have been mostly limited to electrolyte-supported SOCs. Here, we report the first example of the application of perovskite oxide fuel electrodes in novel oxygen electrode supported SOCs (OESCs) with thin YSZ electrolytes, and

demonstrate their excellent performance. The OESCs have $La_{0.8}Sr_{0.2}MnO_{3-\delta}$-$Zr_{0.92}Y_{0.16}O_{2-\delta}$ (LSM-YSZ) oxygen electrode-supports that are enhanced via infiltration of $SrTi_{0.3}Fe_{0.6}Co_{0.1}O_{3-\delta}$, while the fuel electrodes are either Ni-YSZ, STF, STFN, or STFR. Fuel cell power density as high as 1.12 W cm^{-2} is obtained at 0.7 V and 800 °C in humidified hydrogen and air with the STFR electrode, 60% higher than the same cell made with a Ni-YSZ electrode. Electrolysis current density as high as -1.72 A cm^{-2} is obtained at 1.3 V and 800 °C in 50% H_2O – 50% H_2 mode; the STFR cell yields a value 72% higher than the same cell made with a Ni-YSZ electrode, and competitive with the widely used conventional Ni-YSZ-supported cells. The high performance is due in part to the low resistance of the thin YSZ electrolyte, and also to the low fuel electrode polarization resistance, which decreases with fuel electrode in the order: Ni-YSZ > STF > STFN > STFR. The high performance of the latter two electrodes is due to exsolution of catalytic metal nanoparticles; the results are discussed in terms of the microstructure and properties of each electrode material, and surface oxygen exchange resistance values are obtained over a range of conditions for STF, STFN, and STFN. The STF fuel electrodes also provide good stability during redox cycling.

1. Introduction

Ni-based cermet fuel electrodes are widely used in solid oxide electrochemical cells (SOCs) because of their high electrical conductivity, good electrochemical activity, and chemical compatibility with yttria-stabilized zirconia (YSZ) electrolytes. However, Ni-based electrodes have drawbacks for some SOC applications, such as carbon deposition (coking), poisoning by impurities, degradation or failure by redox cycling,[1] and dissolution

of Zr into Ni during electrolysis at high current density.[2] Therefore, there has been a focus on developing alternative fuel electrode materials, typically based on perovskite oxides, that may avoid these problems.[3-6] Oxide fuel electrode performance has recently been substantially improved via "exsolution," where a reducible cation forms catalytic nanoparticles on the oxide surface during cell operation.[7-9]

Unfortunately, issues with co-firing of most perovskite-based fuel electrodes with the YSZ electrolyte have prevented their use in fuel-electrode-supported SOCs. One issue is the low melting point of most perovskite oxides relative to YSZ, which makes it difficult to maintain a porous electrode while densifying the electrolyte. Another issue is that the oxides may chemically react or interdiffuse with YSZ at high sintering temperatures. Thus, oxide-based fuel electrodes have been implemented only in electrolyte supported cells.[10, 11] Cells based on self-supporting zirconia-based electrolytes are certainly useful, but operating temperature is typically $\geq$ 800 °C in order to achieve low electrolyte area specific resistance. Thus, even though exsolution electrodes such as $Sr_{0.95}(Ti_{0.3}Fe_{0.63}Ni_{0.07})O_{3-\delta}$ (STFN) show electrochemical performance comparable to that of Ni-YSZ, fuel cell power density is typically well below 1 W cm^{-2}, much worse than for Ni-YSZ-electrode supported SOCs.[11-13]

Here we demonstrate oxide fuel electrodes in an $La_{0.8}Sr_{0.2}MnO_{3-\delta}$-$Zr_{0.92}Y_{0.16}O_{2-\delta}$ (LSM-YSZ) oxygen electrode supported cell (OESC) with an infiltrated oxygen electrode that helps provide unprecedented cell performance and stability. Among most perovskite electrodes, LSM has good chemical compatibility with YSZ electrolyte[14], permitting them

can be co-fired at high temperature. This design allows for the fuel electrode to be applied after the high-temperature firing of the thin YSZ electrolyte on the oxygen electrode support, providing considerable flexibility in fuel electrode choice. We take full advantage of this to study a range of oxide materials – $Sr(Ti_{0.3}Fe_{0.7})O_{3-\delta}$ (STF), $Sr_{0.95}(Ti_{0.3}Fe_{0.63}Ru_{0.07})O_{3-\delta}$ (STFR), and STFN – and compare them with Ni-YSZ. The latter two oxides utilize B-site doping of STF with Ni and Ru that has been shown to lead to metal catalyst exsolution, improving fuel electrode performance.[10, 15] The electrochemical performance of these cells is investigated under both the fuel cell mode and electrolysis mode. A detailed impedance spectroscopy study is carried out using symmetric-cell data over a range of temperatures and H_2/H_2O ratios, resulting an improved understanding of the electrochemical processes in the different electrodes. Remarkably, the performance of the oxide electrodes is substantially better than that of Ni-YSZ electrodes that have similar microstructure. Results on SOCs with STF-based fuel electrodes operated in electrolysis mode, which has not previously been reported, are presented. The combination of these low-resistance fuel electrodes in the thin-YSZ-electrolyte OESC results in unprecedented cell performance.

2. Results

2.1 Cell Microstructure

All cells had a similar structure and processing scheme. Fig. 1 shows overview cross sectional SEM images of OESCs with STF (a) and Ni-YSZ (b) fuel electrodes – the cells with STFN and STFR are shown in Fig. S1 (ESI†) and they appear identical to the STF cell. The STF-based electrodes thicknesses are 12–15 μm, whereas the Ni-YSZ electrode thickness is ~ 20 μm. An ~ 3-μm-thick GDC interlayer is used in the STF-based electrode

cells to avoid possible reactions with the YSZ electrolyte, but is difficult to resolve from the electrode in Fig. 1(a) because of its porous structure. The YSZ electrolyte has a thickness of about 8–10 μm and appears dense in all cells. Fig. 1 also shows magnified views of the 700 μm thick LSM-YSZ support (c) and 20 μm thick oxygen electrode functional layer (d). Their microstructures are similar – the functional layer has average pore sizes of ~ 1 μm, whereas the support layer has additional larger (5–10 μm) pores designed to help reduce gas diffusion concentration polarization. The $SrTi_{0.3}Fe_{0.6}Co_{0.1}O_{3-\delta}$ (STFC) infiltrated material in the oxygen electrode is not visible in the images because of its relatively small amount and because it appears to uniformly coat the LSM-YSZ surfaces.[16] Nonetheless, a prior study has shown that the infiltrant plays a key role in providing a relatively low and stable oxygen electrode polarization resistance.[16, 17]

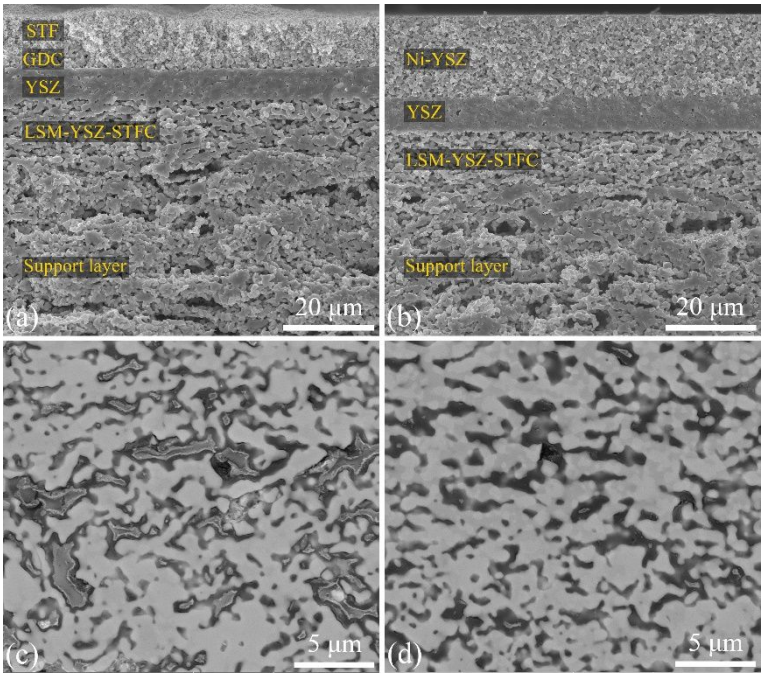

Fig. 1. Fracture cross sectional SEM images giving an overview of the cells with STF (a) and Ni-YSZ electrodes (b). Polished cross-sectional SEM images show higher magnification views of the LSM-YSZ support (c) and the LSM-YSZ functional layer (d).

Fig. 2 shows representative fracture cross-sectional SEM images of the four different fuel electrodes, taken after electrochemical performance testing in 3–50% H_2O humidified H_2 at 800 °C for ~ 2 h. The Ni-YSZ electrode shows the expected porous microstructure (Fig. 2(a)). Ni-YSZ fuel electrodes prepared using the same starting powders, tape-casting formulation, and co-firing procedure have been microstructurally characterized previously using 3D tomography: porosity of ~ 20%, mean particle size of 0.51 μm for Ni and 0.45 μm for YSZ, and an active three-phase boundary (TPB) density L_{TPB} of 7.2 μm^{-2}.[18, 19] The STF (Fig. 2(b)), STFN (Fig. 2(c)), and STFR (Fig. 2(d)) microstructures are porous with well-connected electrode particles, similar to those reported previously for these electrodes in electrolyte-supported cells.[10, 11, 15, 17] STF internal pore surfaces shows mainly micron-scale features, whereas the STFN and STFR electrode surfaces both show uniformly distributed nanoparticles with an areal density of ~ 15–20 μm^{-2}. For comparison, SEM measurements taken from the as-prepared cells (prior to exposure to fuel), see Fig. S2 (ESI†), all show porous micron-scale microstructures similar to Fig. 2(b). This verifies that the nanoparticle exsolution on STFN and STFR occurred upon exposure to fuel during cell testing. Note that the STF phase itself is stable in these electrodes, for the present fuel composition and temperature after the metal nanoparticles are exsolved.[10, 15, 20] Aside from the nanoparticles, the STFN and STFR electrodes are found to have essentially the same microstructure as the STF. Based on stereological measurements made on polished cross-sectional images of the STF-based electrodes (Fig. S3 (ESI†)) porosity values range from 38–40%, specific surface areas *a* are 4.55–4.68 μm^{-1} and solid phase tortuosity factors are 1.24–1.26. Specific values for each electrode are given in Fig. S4 (ESI†).

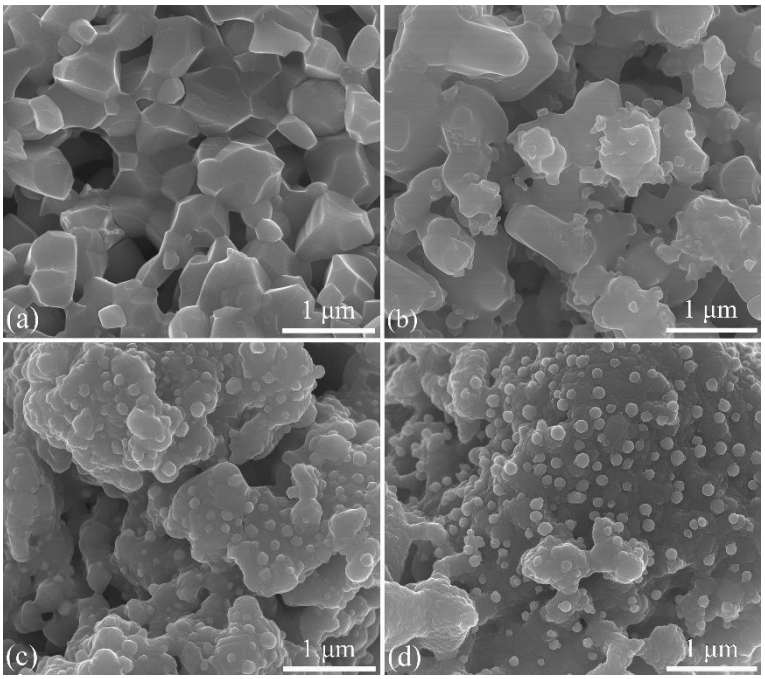

Fig. 2. Fracture cross sectional SEM images showing the microstructures of the Ni-YSZ (a), STF (b), STFN (c), and STFR (d) electrodes after the performance test.

Nanoparticle size distributions, shown in Fig. 3, are similar in STFN and STFR with a mean size of ~ 90 nm in both electrodes. The particle sizes in the present study are slightly higher than those reported in the previous studies (20–70 nm),[10, 15] perhaps because of slightly different testing conditions. Note that prior studies have determined that nanoparticles have typical compositions of ~ 50 mol% Ni – 50 mol% Fe for STFN[15] and ~ 80 mol% Ru – 20 mol% Fe for STFR.[10] The role of the fuel electrode microstructures in determining electrode characteristics is discussed quantitatively in section 3.1.

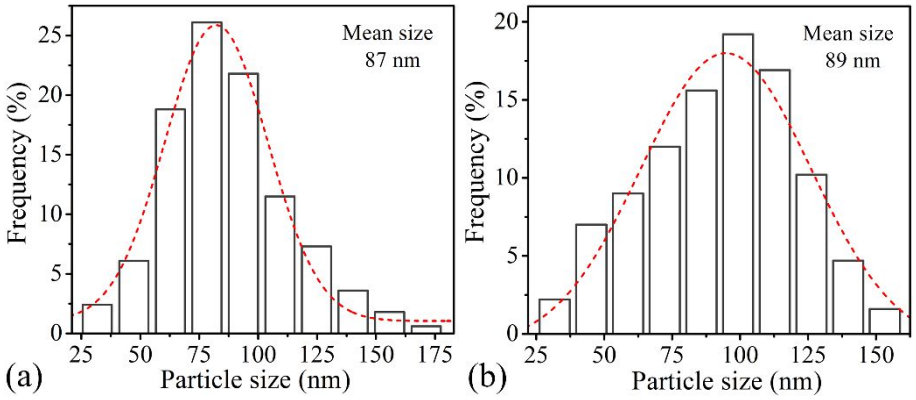

Fig. 3. Fractional size distributions of the Fe-Ni nanoparticles on the STFN electrode (a) and Ru-Ni nanoparticles on the STFR electrode (b).

2.2 Fuel Cell Characteristics

Fig. 4 shows typical electrochemical characteristics of the OESCs with different fuel electrodes in air and 3% and 50% H_2O humidified H_2 fuel ([H_2O] = 3% and 50%). At 3% H_2O, the OCV values at 800 °C are ~ 1.06–1.07 V, similar to OCV values reported previously under these conditions in this cell test setup.[18] At 800 °C, the power density at 0.7 V increases with electrode material in the order: Ni-YSZ (0.7 W cm^{-2}), STF (0.81 W cm^{-2}), STFN (1.01 W cm^{-2}), and STFR (1.12 W cm^{-2}). To our knowledge, these are the highest fuel-cell power densities that have been reported for cells with oxide exsolution anodes[7-9, 21-24]. Similar trends are observed in measurements 800 °C with 50% H_2O (Fig. 4(c)), but at 700 °C with 3% H_2O (Fig. 4(b)) or 50% H_2O ((d)), the STF cell yields lower power density than the Ni-YSZ cell. As discussed in detail in section 2.4, this change can be explained by the increase in STF polarization resistance due to a limitation by hydrogen dissociative adsorption with decreasing temperature.[11] However, the presence of a metallic catalyst in the exsolution materials (Ni-Fe on STFN and Ru-Fe on STFR) results in improved performance compared to STF by accelerating hydrogen adsorption.[10, 15] The apparent limiting current seen in Figs. 4(a) and 4(c) is presumably mainly due to concentration polarization in the thick oxygen electrode; the slightly lower limiting current values for 50 % H_2 may indicate that there is a small contribution to the concentration polarization from the fuel electrode.

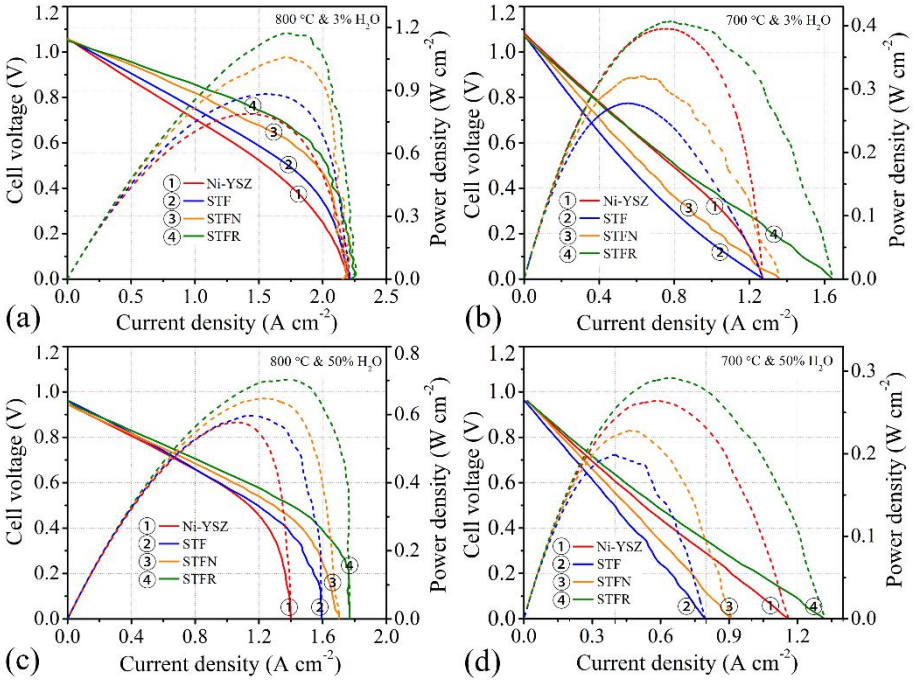

Fig. 4. Voltage and power density versus current density for full cells with different fuel electrodes measured at different conditions. (a) and (c): 800 °C, (b) and (d): 700 °C, (a) and (b) in air and 3% H_2O humidified hydrogen; (c) and (d) in air and 50% H_2O humidified hydrogen.

2.3 Electrolysis Cell Characteristics

Fig. 5 shows the electrolysis voltage *versus* current density at different [H_2O] and temperatures for OESCs with different fuel electrodes. In all cases, the current density at any given voltage increases in the order Ni-YSZ, STF, STFN, STFR; this differs from the fuel cell results in Fig. 4 in that STF is better than Ni-YSZ at all temperatures. At a typical electrolysis condition of 800 °C, 50% H_2O, and 1.3 V, the current density of the STFN cell is 1.45 A cm^{-2} and for the STFR cell 1.72 A cm^{-2}. These values are substantially higher than for the Ni-YSZ cell (1.0 A cm^{-2}) and the STF cell (1.35 A cm^{-2}), and higher than any previous reports for SOECs with oxide fuel electrodes.[25] These values are much higher than the Ni-YSZ cell in this study and Ni-YSZ supported cell with LSM-based electrodes

reported in the literature.[16, 26] These results indicate that the exsolved Ni-Fe and Ru-Fe nanoparticles accelerate not only the fuel cell hydrogen oxidation reaction but also the water-splitting reaction.

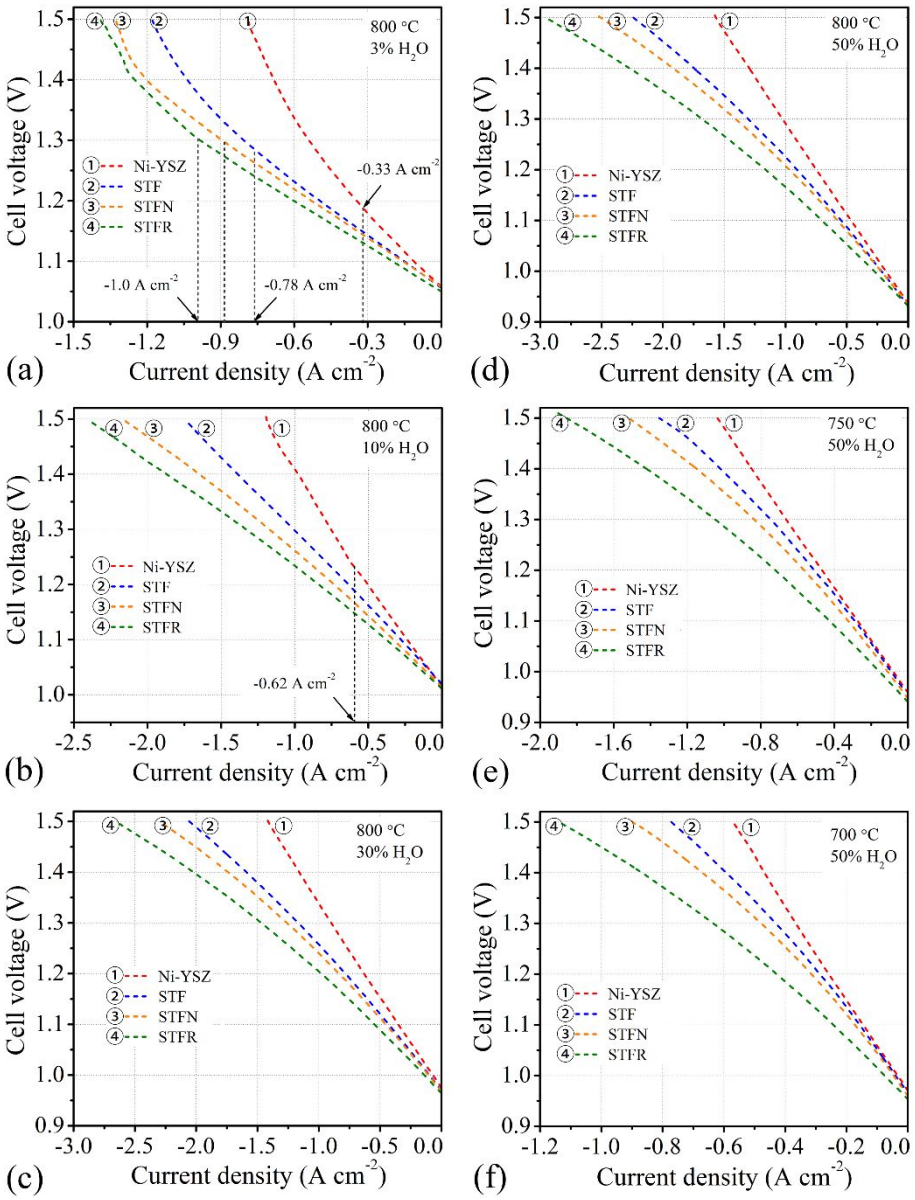

Fig. 5. Electrolysis performance for cells with different fuel electrodes measured at different [H_2O] and different temperatures; (a) 800 ℃, 3% H_2O; (b) 800 ℃, 10% H_2O; (c) 800 ℃, 30% H_2O; (d) 800 ℃, 50% H_2O; (e) 750 ℃, 50% H_2O; (f) 700 ℃, 50% H_2O.

The difference between the STF-based electrodes and Ni-YSZ in Fig. 5 is most pronounced at 3% H_2O, with their performance becoming more similar at higher [H_2O] and

lower temperature. Although 3% and 10% and are unusually low H_2O concentrations for electrolysis, they are shown here to illustrate how the thin fuel electrode in these OESCs minimizes concentration polarization compared to Ni-YSZ supported cells.[18] Indeed, 3% H_2O is the only case where there is a slight indication of limiting current due to the fuel electrode; note that Ni-YSZ shows a smaller limiting current than the STF-based electrodes, presumably due to its larger thickness and lower porosity.

In other cases in Fig. 5, the STF-based cells show a negative curvature of the j-V curves, compared to the more linear dependence for Ni-YSZ. As discussed in section 2.4, the negative curvature may actually be an effect of oxygen enrichment in the thick oxygen electrode with increasing current density, which effectively reduces the polarization resistance.

2.4 Fuel Electrode Electrochemical Characteristics

This section aims to better understand the characteristics of the different fuel electrodes via EIS studies carried out over a range of H_2/H_2O fuel compositions in full cells and symmetrical fuel-electrode cells. Fig. 6(a) and (b) shows the Nyquist and Bode plots measured in 3% and 50% H_2O, respectively, at 800 °C for symmetric cells with the four different electrodes. The high-frequency real-axis intercepts of the impedance arcs are all within a narrow range ($\sim$ 1–1.2 Ω cm^2) and are as expected for the YSZ electrolyte thickness of 0.6 mm. For 3% H_2O, the polarization resistance (R_p) for STF-based electrodes from symmetric cells are all similar and much lower than for the Ni-YSZ electrode (Fig. 6(a)). Increasing the H_2O content to 50% substantially decreases R_p for the Ni-YSZ electrode, while STFN and STFR show lesser decreases and STF increases

slightly. Figs. 6(c) and (d) compare the R_p values versus *inverse* temperature for all the electrodes at 3% and 50% H_2O, respectively, obtained from the real-axis intercepts of EIS data such as that shown in Fig. 6(a). For 3% H_2O, the STF-based electrodes showed much lower R_p values than Ni-YSZ electrode at all the temperatures. For 50% H_2O, the resistance values for STFR and STFN remained similar to the values at 3% H_2O, but the values for STF increased while those for Ni-YSZ decreased. The activation energy calculated from the data in Fig. 6(c) show higher values for STF (0.856 eV) compared to Ni-YSZ (0.625 eV), although STFN (0.826 eV) and STFR (0.796 eV) yielded more moderate values. Increasing [H_2O] to 50% (Fig. 6(d)) yielded a slight decrease in the activation energies of all four electrodes. Fig. 6(e) shows a comparison of the total R_p *versus* [H_2O], taken from data such as that shown in Fig. 6(a), for all the electrodes at 800 °C. For Ni-YSZ, R_p decreases quickly when [H_2O] is increased from 3% to 20%, and then remains stable with further [H_2O] increases. Such a decrease is observed experimentally[27] and expected based on an analysis of the Butler-Volmer equation.[28] R_p values for STF, STFN, and STFR are much lower than for Ni-YSZ at 3% H_2O, decrease with increasing [H_2O] up to 10% H_2O, and then either remain constant (STFN and STFR) or increase slowly (STF) with the increasing [H_2O]. R_p for Ni-YSZ remained substantially higher than for STFN and STFR under this condition, and remained higher even than STF. As shown in Fig. 6(f), the ohmic resistance increased with increasing [H_2O] for STF-based electrodes while it was almost unchanged for Ni-YSZ electrode. Similar changes in ohmic resistance are observed for full cells (see supplemental file, Fig. S5, ESI†). These changes may be explained by a decrease in the conductivity of STF-based materials for lower H_2 partial

pressure.[15]

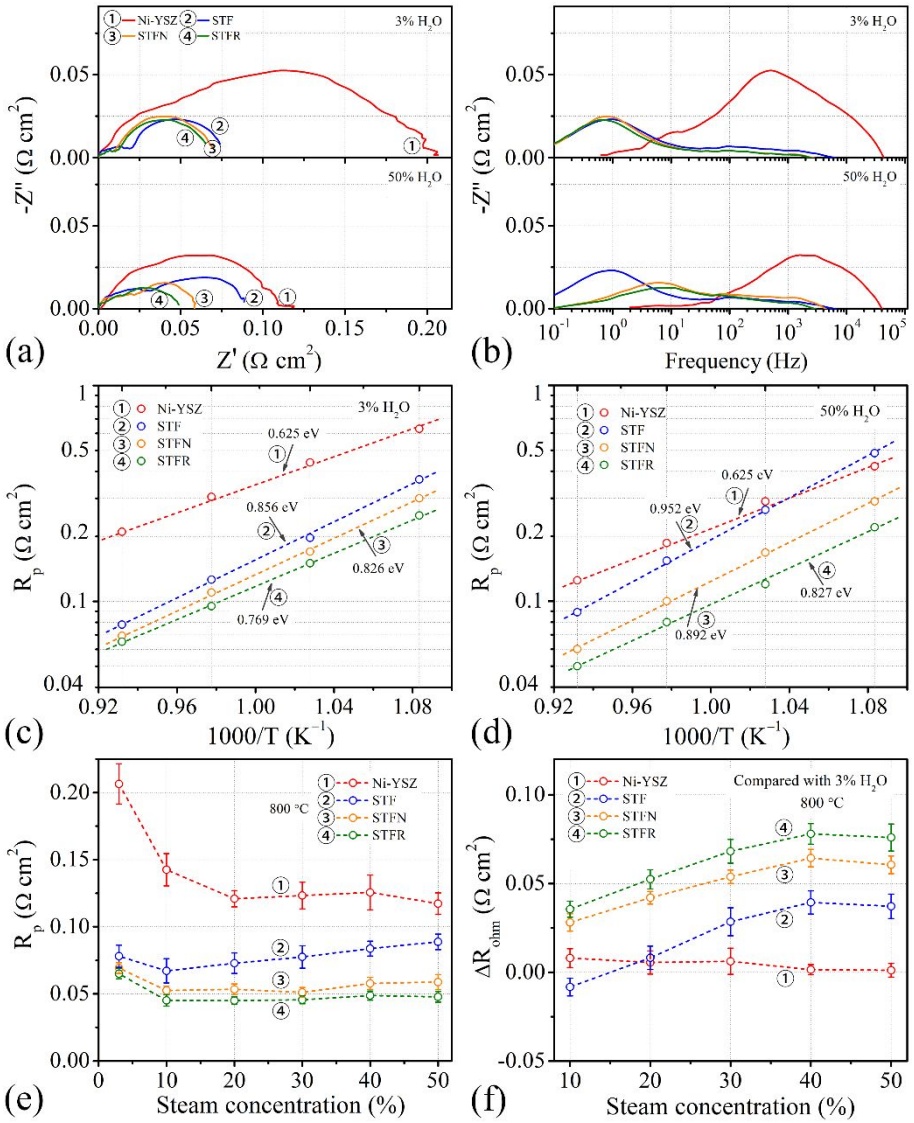

Fig. 6 Typical Nyquist (a) and Bode (b) plots of EIS data measured for symmetric fuel-electrode cells at 3% and 50% H_2O at 800 °C. The high frequency intercepts in the data were set to zero, in order to facilitate comparison of the polarization arcs. Arrhenius plots of the electrode polarization resistance values at 3% H_2O (c) and 50% H_20 (d) measured from the real-axis intercepts on the Nyquist plots as shown in Fig. 4 (a); Evolution of the total R_p (e) and change of R_{ohm} (f)versus inverse [H_2O] for all the electrodes at 800 °C.

Analysis of the symmetric-cell EIS data was done using a distribution of relaxation times (DRT) calculation[29-32] in order to help identify the characteristic distribution of

impedances (*Z*) from various electrochemical processes by timescale. In the DRT calculation, the experimental Z at given frequencies are fitted with eq. 1 to obtain the DRT impedance (Z_{DRT}).

$$Z_{DRT} = R_{ohm} + R_p \int_{-\infty}^{\infty} \frac{\gamma(ln\tau)}{1 + i2\pi f\tau} dln\tau \quad (1)$$

where R_{ohm} is the ohmic resistance, R_p is the polarization resistance, *f* is frequency, τ is the time constant, and $\gamma(ln\,\tau)$ is the distribution function of relaxation times, also written as $\gamma(\tau)$. The resulting *f*-$\gamma(\tau)$ curves are shown in Fig. 7. For Ni-YSZ (Fig. 7(a)), the dominant polarization response is centered at ~ 500 Hz for 3% H_2O and ~ 3000 Hz for 50% H_2O, and a weak response is also observed at ~ 10 Hz. These responses are in general agreement with prior reports for Ni-YSZ,[33, 34] where the higher frequency response is usually associated with the electrochemical charge transfer process and the ~ 10 Hz response is usually associated with gas diffusion. The present 10 Hz response is much smaller compared to typical anode-supported cells, presumably due to much-reduced gas diffusion concentration polarization for the present relatively thin electrodes. The response at ~ 10^4 Hz seen for Ni-YSZ may be related to YSZ grain boundaries.[34] For all the STF-based electrodes (Fig. 7(b) to (d)), the main polarization response is centered at ~ 1 Hz and, based on prior results,[11] can be attributed to H_2 adsorption and/or the reaction between H_2 and surface O^{2-}. The weaker responses in the 100 – 1000 Hz range can be attributed to O^{2-} transport in the oxide electrode and/or O^{2-} transfer from electrode into electrolyte.

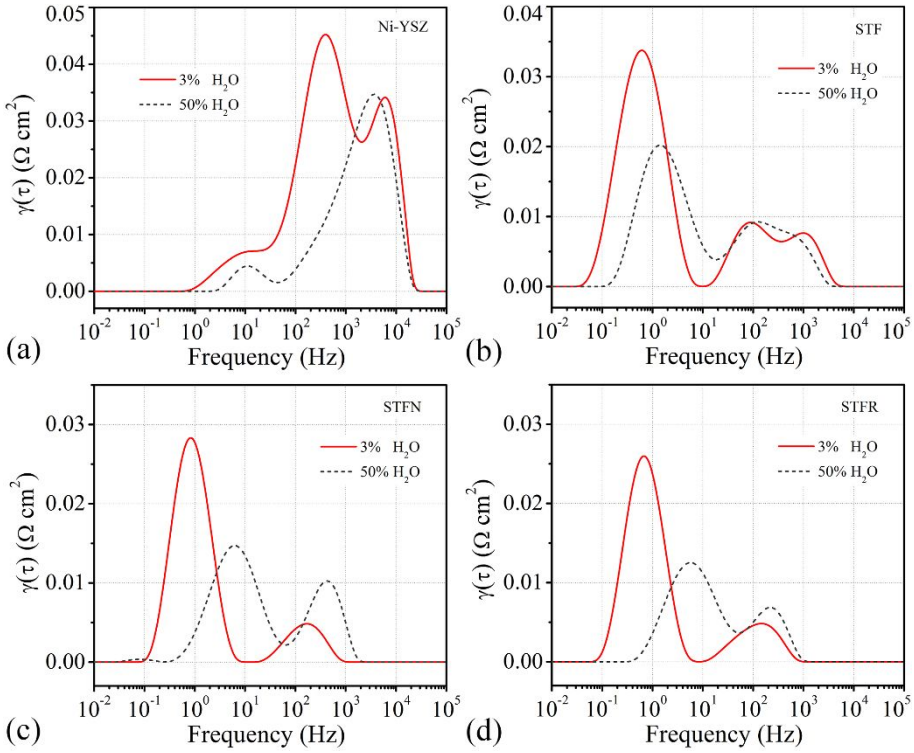

Fig. 7 DRT of the EIS spectra for symmetrical cells with (a) Ni-YSZ, (b) STF, (c) STFN, and (d) STFR in 97% H_2 + 3% H_2O and 50% H_2 + 50% H_2O at 800 °C.

A similar equivalent circuit model (Fig. S6 (ESI†)) is used for all of the electrodes for complex nonlinear least square (CNLS) fitting of the EIS data. The porous electrode is represented by a simplified transmission line model including the ionic conductivity $R_{O^{2-}}$ of the electrode and the hydrogen oxidation reaction at the electrode/gas interface$R_{elec/gas}$ $Q_{elec/gas}$, along with an $R_{int}Q_{int}$ element representing an interfacial process and $R_{H_2}Q_{H_2}$ representing hydrogen adsorption. The fitted EIS curves are shown in Fig. S7 (ESI†); the resistance values of individual processes obtained from the fits are shown in Fig. 8.

The results in Fig. 8 can be understood as follows. The oxygen transport resistance $R_{O^{2-}}$ (Fig. 8 (a)) for all the STF materials is similar, and lower than for Ni-YSZ; faster oxygen transport in STF than YSZ is consistent with the slightly higher oxygen diffusion coefficient (D_{chem}) of STF (~ 2.2×10^{-7} cm^2 s^{-1} at 800 °C in

air)[17, 35] than YSZ (~ 1×10^{-7} cm^{2}s^{-1}).[36, 37] The slight increase in $R_{O^{2-}}$ in the STF-based electrodes on going from 3% to 50% H_2O makes sense because of the expected reduction in the oxygen vacancy concentration. The surface reaction resistance $R_{elec/gas}$ (Fig. 8(b)) is substantially lower for the STF-based electrodes compared to Ni-YSZ, perhaps because they are mixed conductors allowing hydrogen oxidation over the entire porous electrode surface area, whereas the reaction is confined to three-phase boundaries for Ni-YSZ. $R_{elec/gas}$ is very much reduced in STFN and STFR compared to STF. This can be understood based on previous studies[10, 15] of STFN and STFR electrodes that showed that a high density of nanoparticles formed on the oxide surfaces after exposure to fuel conditions: the particles were metallic alloys with approximate compositions $Ni_{0.5}Fe_{0.5}$ and $Fe_{0.2}Ru_{0.8}$, respectively. Fig. 2 shows that the present STFN and STFR electrodes showed such surface nanoparticles, but STF did not. This suggests that the surface reaction is promoted by the presence of the exsolved catalysts. The hydrogen adsorption resistance R_{H_2} (Fig. 8(c)) on STF is much higher than on Ni-YSZ, presumably because STF lacks a metallic catalyst that promotes H_2 dissociative adsorption.[11, 15] This idea is supported by the observation that STFN and STFR have lower R_{H_2} values than STF, again presumably due to the presence of exsolved metal catalysts. The interfacial resistance R_{int} (Fig. 8(d)) probably represents oxygen transport across the electrode/electrolyte interface for the STF-based electrodes, and probably grain boundary transport for Ni-YSZ. The value is similar for the all the

STF-based electrodes, reasonable because of their very similar compositions, and larger for Ni-YSZ.

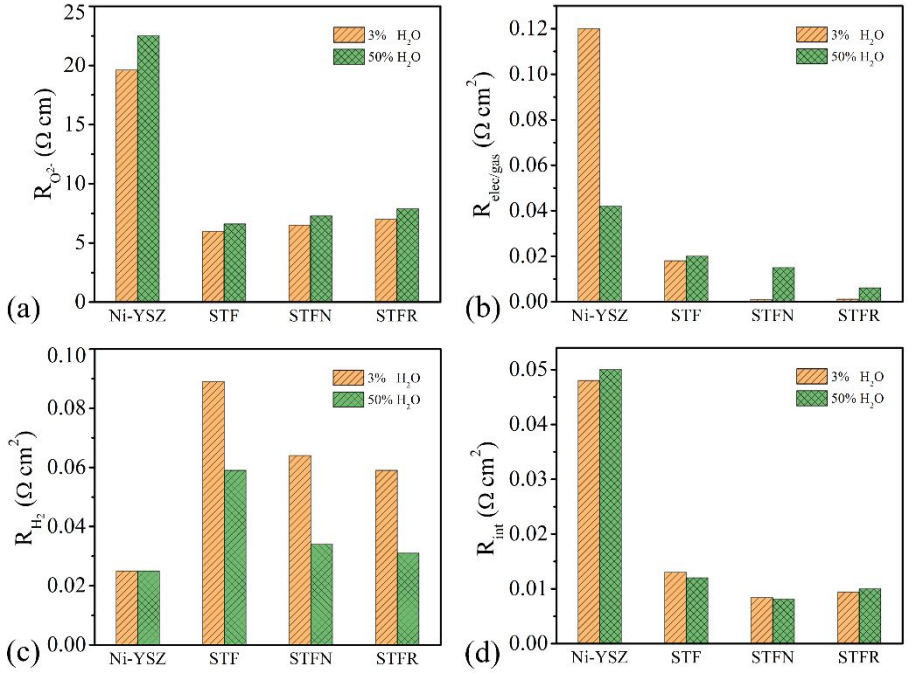

Fig. 8 Resistance values obtained from EIS fittings at 800 °C.

Finally, a comparison of the symmetric-cell EIS data (Fig. 6) with the full-cell EIS data at 800 °C (Fig. S8 and S9 (ESI†)) shows very similar responses. A comparison of the polarization responses in the full cells and the symmetric cells suggests that the oxygen- and fuel-electrode polarization resistances have similar magnitudes at 800 °C. However, it is generally expected that the oxygen electrode resistance, which has a relatively high activation energy, will be dominant at lower temperature.

2.5 Stability, reversibility, and redox stability

It is important to establish that the present results represent stable cell performance. Although extended life tests are beyond the scope of the present work, short life test results are shown for fuel cell (Fig. 9(a)), electrolysis (Fig. 9(b)),

and reversible operation (Fig. 9(c)). Fig. 9(a) shows that during a fuel cell test carried out at 750 °C and 0.5 A cm^{-2}, the cell voltage is reasonably stable, initially increasing slightly from 0.66 V before decreasing gradually over ~ 300 h to 0.69 V. Fig. 9 (b) shows that during an electrolysis test at 750 °C and –0.5 A cm^{-2}, the cell voltage increases from 1.18 V over the first ~ 50 h but appears to be stabilizing at 1.23 V by the end of the test. Fig. 9 (c) shows the voltage versus time of a cell alternating every 6 h between electrolysis operation at –0.5 A cm^{-2} and fuel cell operation at +0.5 A cm^{-2}, at 750 °C and 50 % H_2O – 50 % H_2. After some voltage degradation over the first ~ 50 h, the cell voltages appear to stabilize.

Redox cycling was also carried out, since a key potential advantage of replacing Ni-YSZ with oxides is to avoid cell damage caused by Ni oxidation/reduction cycles.[38, 39] Fig. 9(d) shows the results of a redox cycling fuel-cell test where the fuel electrode was alternately supplied with humidified H_2 for 1 h and air for 1 h, with a short intervening gas purge. The initial fuel cell voltage at 750 °C and 0.5 A cm^{-2}, 0.72 V, increases slightly during the first 3 redox cycles, then decreases slightly, and appears to be gradually stabilizing at 0.71 V after ten total cycles. EIS data (Fig. S10 (ESI†)) from the cell before and after redox cycling testing showed that there was a slight increase in R_{ohm} and R_p. This is probably just a normal break-in seen at the beginning of any life test, given that the fracture cross-sectional SEM images taken after the redox cycling test (Fig. S11 (ESI†)) showed no delamination, cracking, or other microstructure changes. Prior results indicate that redox cycling damage is exacerbated for electrodes with large volume changes (e.g. Ni-YSZ) and large thickness (anode supported cells).[39] The present results showing no redox

cycling damage are thus reasonable given that the present STF electrodes have little volume change and are relatively thin. It will be interesting in the future to observe redox cycling of cells with STFN and STFR electrodes, because prior results suggest that redox cycling of exsolution electrodes can restore degraded performance.[40]

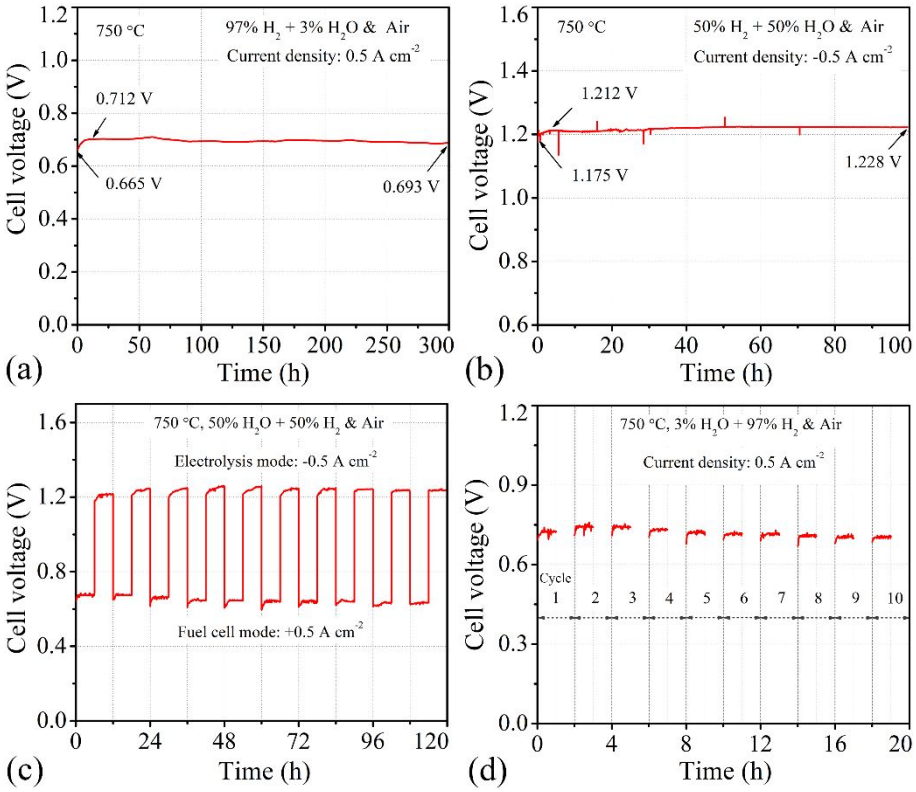

Fig. 9 Cell voltage versus time for the cell with STF electrode measured at 750 °C (a) in air and 3% H_2O +97% H_2 with j = 0.5 A cm^{-2} in fuel cell mode; (b) in air and 50% H_2O +50% H_2 with j = -0.5 A cm^{-2} in electrolysis mode; (c) in air and 50% H_2O +50% H_2 with j = ±0.5 A cm^{-2} under SOFC/SOEC reversible condition. (d) Cell voltage versus time during the redox cycling.

3. Discussion

3.1 Electrode electrochemical characteristics

The present STFN and STFR fuel electrodes yield R_p values near 0.05 Ω cm^2 at 800 °C over a wide range of H_2/H_2O compositions (Fig. 6). These values are lower than in

prior reports of oxide fuel electrodes with catalyst exsolution. For example, comparing values measured at 800 °C in 3% H_2O humidified H_2, a $Pr_{0.8}Sr_{1.2}(Co,Fe)_{0.8}Nb_{0.2}O_{4+\delta}$ electrode with exsolved Co-Fe nanoparticles yielded R_p = 0.44 Ω cm^2,[21] whereas a $Sr_2FeMo_{0.65}Ni_{0.35}O_{6-\delta}$ electrode with exsolved Ni-Fe nanoparticles yielded R_p = 0.163 Ω cm^2.[41] Both values are much higher than those for the present STFN and STFR electrodes. Furthermore, they provide better electrochemical performance than the present Ni-YSZ electrodes.

Here we discuss the electrochemical characteristics of the Ni-YSZ and STF-based electrodes, including the impact of their microstructures. Two different transmission line model (TLM) expressions are used, one for Ni-YSZ that accounts for three-phase boundaries (TPBs) and one for STF-based electrodes that accounts for surface exchange. Ni-YSZ fuel electrodes prepared using the same materials, tape casting, and firing procedures have been microstructurally characterized previously using 3D tomography: porosity of ~ 20%, mean particle size of 0.51 μm for Ni and 0.45 μm for YSZ, and an active TPB density L_{TPB} of 7.2 μm^{-2}.[18, 19] This data together with the materials' transport properties can be used to calculate R_P using the TLM expression:[42]

$$R_P = \sqrt{\frac{R_{LS}}{\sigma_{ion} L_{TPB}}} \coth\left(L\sqrt{\frac{L_{TPB}}{\sigma_{ion} R_{LS}}}\right) \quad (2)$$

where L is the electrode thickness (20 μm), and σ_{ion} the YSZ effective ionic conductivity given by the conductivity (~ 0.01 S cm^{-1} at 800 °C) times the YSZ solid fraction, 60%, and divided by the YSZ tortuosity, 1.8. Reported values of the length-specific TPB resistance R_{LS} range from ~ 10000 to 30000 Ω cm at 800 °C depending on the gas composition,[43]

yielding R_P = 0.06–0.11 Ω cm^2, slightly lower than the measured values shown in Fig. 6. Note that these electrodes work in the "thick electrode" limit, *i.e,* electrochemical processes occur primarily within a layer much thinner than the electrode, such that increasing L does not reduce R_P.

The R_P value of a porous mixed ionic/electronic conducting electrode (MIEC) can be related to the materials' transport properties and the electrode microstructure using a TLM expression:[42]

$$R_P = \sqrt{\frac{R_s}{\sigma_{ion} a}} \coth\left(L\sqrt{\frac{a}{\sigma_{ion} R_s}}\right) \quad (3)$$

Where R_S is the surface oxygen exchange resistance, L is the electrode thickness (12–15 μm), a is the electrode surface area (4.6 μm^{-1}), and the STF effective ionic conductivity σ_{ion} is given by the ionic conductivity times the anode solid fraction, 0.6–0.62, and divided by the solid-phase tortuosity, (1.24–1.26). This is similar in form to eq. 2, with TPB length replaced by surface area, and TPB line-specific resistance replaced by surface resistance. Since an ionic conductivity has been measured for STF at 650 °C,[44] 0.025 S cm^{-1}, we carry out the calculation at this temperature (note that after exsolution the oxide matrix composition of STFN and STFR becomes approximately $Sr(Ti_{0.3}Fe_{0.7})O_3$,[10, 15] so the same value can be used for STF, STFN, and STFR). For the above parameters, it is found that eq. 3 can be approximated well in the "thin electrode" limit as:

$$R_p = R_s/aL \quad (4)$$

where $aL = 55$ is the electrode surface area normalized to the electrode size. Thus, values of surface resistance for the oxide electrodes can be obtained to good approximation directly from Fig. 6(c) and (d) using eq. 4. Fig. 10 plots the resulting R_S values versus temperature for the two fuel compositions. The only prior measurement of the surface

oxygen exchange resistance of an oxide fuel electrode was for thin-film STF with the same composition, yielding R_S values that range from 25 Ω cm^2 at 650 °C to 6 Ω cm^2 at 800 °C.[44] These values are somewhat higher than the values in Fig 10, *e.g.*, R_S = 4.7 Ω cm^2 for STF at 800 °C in 50 % H_2O, probably due to the lower H_2 and H_2O partial pressures in the prior work. The activation energy of R_S is 0.87 eV for 3% steam and 0.95 eV for 50% steam, compared to the value measured in Ref. 44, 0.92 eV. Fig. 10 confirms that the exsolution electrodes have lower intrinsic oxygen surface exchange resistances than STF, especially at the higher steam content, e.g., 3.05 Ω cm^2 for STFN, and 2.45 Ω cm^2 for STFR at 800 °C. Finally, eqs. 3 and 4 predict that increasing the thickness of the STF-based electrodes is expected to decrease R_P.

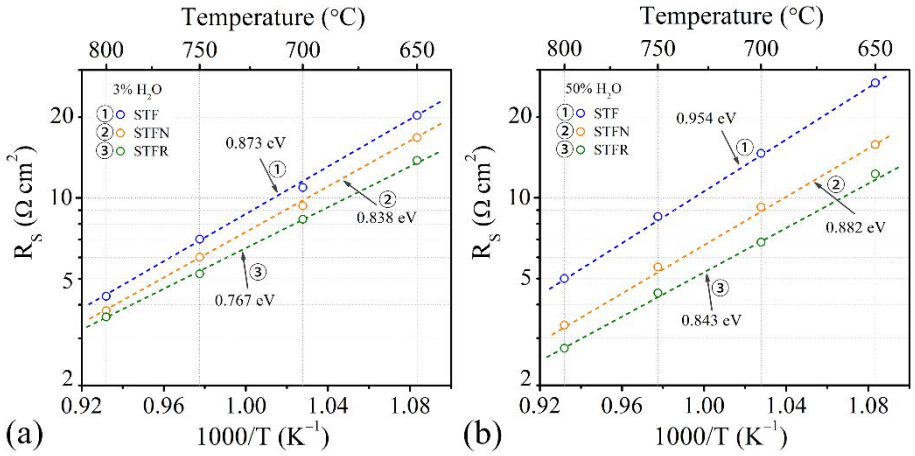

Fig. 10. Surface oxygen exchange resistance R_S versus inverse temperature for the two fuel compositions, obtained using eq. 4 with the data in Figs. 6(c) and 6(d).

The present STF-based electrodes provide better electrochemical performance than the Ni-YSZ electrodes. This can be ascribed to the larger reaction area of the STF-based MIEC electrode materials compared to the limited TPB reaction area in Ni-YSZ; this argument is often used to explain the good performance of MIEC oxygen electrodes compared to LSM-YSZ. However, the above TLM expressions for the two electrode types

show that this argument depends upon the actual microstructures – primarily the magnitudes of a and L_{TPB}. Thus, the most that can be said is that for the present microstructures, which were obtained using fairly standard solid oxide cell processing yielding particle sizes of ~ 0.5–1.0 μm, lower R_P values are obtained for the STF-based electrodes. A microstructure effect also probably explains the very low R_P values of the present STF-based electrodes; a factor of ~ 2 times lower than in prior reports.[10, 15] In these prior studies, the electrodes were fired at 1150 °C yielding a porosity of ~ 23% and specific surface area of ~ 2.12 μm^{-1},[10, 15] much lower than the present case where the electrodes were fired at a lower temperature of 1050 °C yielding 38–40% porosity and a 4.55–4.68 μm^{-1}. The higher a value results in R_P values ~ 2 times lower in eq. 4.

The only case where the STF electrode showed worse performance than Ni-YSZ was in fuel cell mode at lower temperature (Fig. 4 (b) and (d)). Also, STF is only slightly better than Ni-YSZ in 50% H_2O–50% H_2. These trends are consistent with prior results suggesting that STF becomes strongly limited by hydrogen adsorption at lower temperature and low H_2 content.[11] In contrast, in electrolysis mode, the STF-based electrodes are superior to Ni-YSZ at all temperatures. This is due in part to the positive curvature of the j-V curves for STF-based electrodes, compared to the more linear curves for Ni-YSZ. One possible explanation for this curvature is that the H_2/H_2O mixture within the electrode becomes increasingly enriched with H_2 as J increases; especially for STF, both R_P and ohmic resistance decreases with increasing H_2 content, as shown in Fig. 6. As discussed in prior work, increasing the H_2 content helps to overcome the H_2 adsorption rate limitation, thereby decreasing R_P.[11]

STF lacks a metallic catalyst such as Ni that can promote H_2 adsorption. The improved electrochemical performance of STFN and STFR electrodes compared with STF is presumably explained by the catalytic activity of exsolved nanoparticles on oxide anode surfaces.[13, 25, 45-47] The presence of Ni-Fe and Ru-Fe nanoparticles on the STF surfaces can promote hydrogen dissociation and water splitting, with adsorbed atomic hydrogen spilling over onto the oxide surface for subsequent electrochemical reaction, similar to composite fuel electrodes such as Ni-YSZ.[11] Given that the nanoparticle densities and sizes are similar for both compositions (Fig. 3), the better performance of the STFR electrodes suggests that Ru-Fe is a more effective catalyst than Ni-Fe. The nanoparticle effect is especially pronounced at lower temperatures, as indicated by the lower activation energy of R_P for STFN and STFR in Fig. 6(c) and (d)). Furthermore, the R_p of STF increased with increasing [H_2O], whereas the nanoparticle effect in STFN and STFR electrodes reduced R_P and eliminated its increase with [H_2O].

3.2 Cell performance

OESCs have been extensively developed previously by Siemens-Westinghouse,[48, 49] although these cells had thicker electrolytes and were designed for higher operating temperatures than the present cells. OESCs with thin electrolyte prepared by sputter deposition on LSM supports were also reported.[50] These cells yielded a maximum fuel-cell power density of 0.8 W cm^{-2}, considerably less than the present cells. S. R. Wang et al. reported the OESCs prepared by tape casting with thin $Zr_{0.89}Sc_{0.1}Ce_{0.01}O_{2-\delta}$ (SSZ) electrolytes.[51] However, the cells showed a maximum fuel-cell power density of 0.48 W cm^{-2} at 800 °C even the SSZ electrolyte has much higher conductivity than YSZ.

Most oxide-based fuel electrodes have been implemented in electrolyte supported cells,[52] with only few reports in OESCs and no reports in fuel-electrode supported cells. An OESC with $La_{0.75}Sr_{0.25}Cr_{0.5}Mn_{0.5}O_{3-\delta}$ (LSCM) fuel electrode yielded a power density of 0.25 W cm^{-2} at 800 °C and 0.7 V.[53] Cells with Ru-CeO_2 infiltrated $Sr_{0.88}Y_{0.8}TiO_{3-\delta}$-YSZ (SYTO-YSZ) fuel electrodes yielded power density of 0.48 W cm^{-2} at 800 °C and 0.7 V.[54] The present OESCs yielded substantially better fuel cell performance than in these previous reports; as discussed above, this is due at least in part to the very low polarization resistances achieved by the present STF-based electrodes. In comparison to electrolyte-supported fuel cells with oxide-based fuel electrodes, the present result show substantially higher power density.[15] While this is due in large part to the lower resistance of the present thin electrolytes, the results in section 3.1 show that it is also due to the very low polarization resistances achieved by the present STF-based electrodes.

There have been a number of prior reports of solid oxide electrolysis using perovskite-oxide and exsolution fuel electrodes[55-61] although none of these have been in OESCs and none have shown performance comparable to the present cells. However, the present results appear to be the first direct comparison of the electrolysis performance of cells with oxide-based and Ni-YSZ electrodes. The best-performing OESC (with the STFR-electrode) yielded an electrolysis current density of 1.72 A cm^{-2} at 1.3 V, 800 °C, and 50% H_2O, comparable to that of a Ni-YSZ supported cell with STFC infiltrated LSM-YSZ electrode under the same conditions, 2.0 A cm^{-2}.[16] Furthermore, the present OESCs have been shown to provide excellent electrolysis performance at low [H_2O], due to the relatively fast gas diffusion in the thin fuel electrode, which could allow electrolysis with higher utilization.

4. Conclusions

The key findings and conclusions of this study are as follows:

(1) Oxygen electrode supported cells (OESCs) are described that utilize a combination of high performance infiltrated LSM-YSZ oxygen electrode and STF-based exsolution fuel electrodes with a thin YSZ electrolyte to provide the best reported performance for oxygen electrode supported cells, and the best reported performance of cells with ceramic-based fuel electrodes.

(2) Cells with STF-based fuel electrodes yield higher current density in fuel cell and electrolysis modes than cells with Ni-YSZ electrodes. The best values are obtained with STFR – a fuel cell power density of 1.1 W cm^{-2} at 0.7 V and 800 °C in humidified hydrogen and air, and an electrolysis current density of 1.72 A cm^{-2} at 50% H_2O and 800 °C.

(3) The cell performance is limited by the ohmic resistance and both electrodes at 800 °C, but is dominated more by the oxygen electrode at lower temperature. In order to achieve improved cell performance at lower temperatures, it will be helpful to reduce the electrolyte resistance, e.g. by utilizing improved current collectors and/or a thinner electrolyte, and reducing electrode polarization resistance, e.g., by improving electrode microstructure.

(4) The STF-based electrodes show substantially lower polarization resistance than Ni-YSZ electrodes for most operating conditions, and their resistance shows less variation with fuel composition than Ni-YSZ.

(5) Compared with STF electrodes, STFN and STFR electrodes show significant performance enhancement, explained by the observed nanoparticle exsolution. The

nanoparticle effect was especially pronounced at lower temperatures and higher steam (lower H_2) fuel compositions.

(6) The transmission line model combined with quantitative microstructural data provides values of the intrinsic surface resistances of the STF, STFN, and STFR electrodes over a range of temperatures and gas compositions.

(7) OESCs show excellent steam electrolysis performance in low-H_2O fuel because of the reduced gas diffusion limitation of the thin fuel electrode. This could provide an advantage over fuel-electrode supported cells in case of high steam utilization.

(8) The present OESCs with STF fuel electrode show good short-term stability in fuel cell, electrolysis, and reversible operation, as well good redox cycling stability. Longer life-tests are needed in the future to establish long-term stability.

5. Experimental procedures

5.1 Materials synthesis

The solid-state reaction method was used to synthesize the $Sr(Ti_{0.3}Fe_{0.7})O_{3-\delta}$ (STF), $Sr_{0.95}(Ti_{0.3}Fe_{0.63}Ni_{0.07})O_{3-\delta}$ (STFN), and $Sr_{0.95}(Ti_{0.3}Fe_{0.63}Ru_{0.07})O_{3-\delta}$ (STFR) powders. A-site deficient composition was chosen since prior work has shown that A-site deficiency promotes B-site metal exsolution and results in a more stoichiometric perovskite after exsolving B-site transition metals, which can improve the electrochemical performance significantly.[62, 63] $SrCO_3$ (Sigma-Aldrich), TiO_2 (Alfa Aesar), Fe_2O_3 (Alfa Aesar), RuO_2 (Sigma-Aldrich), and $Ni(NO_3)_2{\cdot}6H_2O$ (Sigma-Aldrich) were the starting materials. Stoichiometric amounts of the powders were ball milled in ethanol for 24 hours with zirconia balls as milling medium. The mixed

powders were then dried and calcined at 1100 °C for 10 hours. The resulting powders were subsequently ball milled in ethanol for another 48 hours as described above and dried.

5.2 Cell fabrication

LSM-YSZ supported half cells were prepared by tape casting with 38.5 wt.% LSM + 41.5 wt.% YSZ + 8 wt.% starch (pore former) + 12 wt.% Graphite (pore former) as the support layer, 38.5 wt.% LSM + 38.5 wt.% YSZ + 23 wt.% Graphite (pore former) as the oxygen electrode functional layer, and YSZ as the electrolyte. In order to reduce the firing temperature, 3 mol% Fe_2O_3 was added in the electrolyte as the sintering aid. Then the cells were co-fired at 1225 °C for 2 h. The slurry formulations and firing conditions were optimized to yield cells without significant curvature. Next, in order to prevent any reactions between YSZ electrolyte and STF-based electrodes, a $Gd_{0.1}Ce_{0.9}O_{2-\delta}$ (GDC) interlayer was screen printed on the YSZ electrolyte and then fired at 1175 °C for 2 h. STF, STFN, and STFR inks were prepared by mixing the powders and binder (V-737, Heraeus) with weight ratio of 1 : 1.2 in a three-roll mill. Then the fuel electrodes were screen printed onto the GDC interlayer and calcined at 1050 °C for 4 h.

For comparison, LSM-YSZ supported full cells with Ni-YSZ electrode were also fabricated. For this type of cell, 50 wt.% NiO + 50 wt.% YSZ fuel electrode[18, 19] was co-fired with the electrolyte, oxygen electrode functional layer, and support layer at 1225 °C for 2 h (without GDC interlayer). Although this procedure is different than that noted above for the STF-based electrodes, it is used because it has been previously shown to yield

excellent anode microstructure and performance,[18, 19] and also because it produces similar feature sizes. For infiltrated full cells, ~ 4 mg $SrTi_{0.3}Fe_{0.6}Co_{0.1}O_{3-\delta}$ (STFC) was infiltrated into the LSM-YSZ support and electrode functional layer to improve its performance. Because the LSM-YSZ electrodes are first co-fired with the YSZ electrolyte at 1225 °C. This condition, necessary to obtain dense YSZ, is not ideal for the LSM-YSZ electrode. The support side was infiltrated with 0.25 mol L^{-1} STFC precursor solution using fluid of ~25 μL. The infiltrate was decomposed by heating to 450 °C for 0.5 h, leaving oxides of the respective metal ions. After 4 infiltration steps, the cells were fired at 800 °C for 1 h to form STFC. The preparation process for the STFC precursor solution can be found in our previous study.[16]

Symmetric cells with different fuel electrodes were also prepared to investigate the electrode performance. YSZ electrolyte pellets (~ 0.6 mm in thickness, ~ 15 mm in diameter) were prepared by tape casting. Similar with the full cells, 3 mol% Fe_2O_3 was added in the electrolyte as the sintering aid and the pellets were fired at 1225 °C for 2 h. Prior reports have shown that the resulting electrolytes provide the correct ionic conductivity and open circuit voltage, indicating that the properties are not compromised.[18, 19] Then GDC interlayer was screen printed on both sides of the electrolyte pellets followed by firing at 1175 °C for 2 h. Finally, the STF-based fuel electrodes were screen printed on the GDC interlayer and calcined at 1175 °C for 2 h. NiO-YSZ electrodes were co-fired with the electrolyte at 1225 °C for 2 h. In all cases, the total effective area of the fuel electrode is 0.5 cm^2.

5.3 Electrochemical characterization

For the full cell testing, a gold grid (Heraeus Inc., Pennsylvania) was screen printed onto the STF-based fuel electrode for current collection since the conductivity of these materials is relatively low.[7] The Ni-YSZ electrodes not need the current collector. The cells were sealed onto alumina tubes with silver paste (DAD-87, Shanghai Research Institute of Synthetic Resins). For fuel cell testing, 100 sccm humidified H_2 (97% H_2 + 3% H_2O) was supplied to the fuel electrode while 150 sccm air was supplied to the LSM-YSZ-STFC support, in the temperature range of 700–800 °C. For electrolysis testing, the oxygen electrode was exposed to air (150 sccm) while 100 sccm H_2 flowed through a heated H_2O-containing bubbler was supplied to the fuel electrode. In this study, the water in the bubbler was controlled at different temperatures, entraining different volume fraction water (3–50%) in the H_2 flow. Current–voltage curves were measured at 20 mV increments over the relevant voltage ranges for fuel cell and electrolysis operation. The EIS measurements were conducted using an IM6 Electrochemical Workstation (ZAHNER, Germany) with a 20 mV AC signal in the frequency range of from 0.1 Hz to 100 kHz (under OCV condition). For the symmetric cells, gold contact grids were screen printed on both sides to facilitate current collection for the STF-based electrodes. The EIS curves under different temperatures and different [H_2O]s were tested as mentioned above. In all cases, prior to testing the cells were heated up to 800 °C with fuel electrode exposed in Ar, and maintained at that temperature for 2 h after switching the gas to room temperature humidified H_2. DRT calculations for the symmetrical cells were performed with DRT tools, a GUI implemented in MATLAB.[64] After the performance testing, cell microstructures were examined via scanning electron microscopy SEM (Hitachi SU8030).

5.4 Redox cycling test and SOFC/SOEC reversible cycling test

The redox stability test for the cell with STF electrode was performed under the SOFC mode. The configuration of the redox cycling test is shown in Fig. S12 (ESI†). In this protocol, the cell was firstly heated to 800 °C under the same procedures as shown above. Then, the cell is cooled down to 750 °C and kept at this temperature. The cell voltage was measured at a constant current density of 0.5 A cm^{-2}. After 1 h test, current and fuel were stopped. In order to avoid the potential explosion dangers, 50 sccm argon was supplied to the fuel electrode for 10 min to vent the residuary hydrogen in the setup chamber. Then, 100 sccm air was supplied to the fuel electrode for 20 min oxidation. Next, 50 sccm argon was supplied for 10 min to vent the residuary air before suppling the hydrogen. After 20 min reduction, the cell voltage for the next cycle was measured at the same condition shown above. EIS measurements were made before and after the 10 cycles tests with no applied potential.

For the SOFC/SOEC reversible cycling test, the temperature was kept at 750 °C. The oxygen electrode was exposed to air (150 sccm) while 100 sccm 50% H_2O + 50% H_2 was supplied to the fuel electrode. Current density was set at 0.5 A cm^{-2} while the current direction was switched every 6 hours, giving a 12-hour period. The cell voltage was measured.

Acknowledgements

The authors gratefully acknowledge financial support by the Department of Energy grant # DE-SC0016965. Initial development of the oxygen-electrode-supported cells was done under support from the National Science Foundation (DMR-1912530), and

electrochemical performance was analyzed under support from Department of Energy (DE-EE0008437). Shan-Lin Zhang gratefully acknowledges the scholarship from the State Scholarship Fund of China Scholarship Council (201606285002). The authors at Xi'an Jiaotong University acknowledge National Natural Science Foundation of China (Grant No. 51602248) for support of stability test. This work made use of the EPIC facility of Northwestern University's NUANCE Center, which has received support from the Soft and Hybrid Nanotechnology Experimental (SHyNE) Resource (NSF ECCS-1542205); the MRSEC program (NSF DMR-1121262) at the Materials Research Center; the International Institute for Nanotechnology (IIN); the Keck Foundation; and the State of Illinois, through the IIN. This work made use of the MatCI Facility which receives support from the MRSEC Program (NSF DMR-1720139) of the Materials Research Center at Northwestern University.

Reference

1. A. Atkinson, S. Barnett, R. J. Gorte, J. T. S. Irvine, A. J. McEvoy, M. Mogensen, S. C. Singhal and J. Vohs, *Nature Mater.*, 2004, **3**, 17-27.

2. M. Chen, Y.-L. Liu, J. J. Bentzen, W. Zhang, X. Sun, A. Hauch, Y. Tao, J. R. Bowen and P. V. Hendriksen, *J. Electrochem. Soc.*, 2013, **160**, F883-F891.

3. A. Das, S. Kumar, S. Kumar and S. Omar, *Electrochim. Acta*, 2020, **354**.

4. A. A. Yaremchenko, J. Macias, A. V. Kovalevsky, B. I. Arias-Serrano and J. R. Frade, *J. Power Sources*, 2020, **474**.

5. Y. Ji, Y.-H. Huang, J.-R. Ying and J. B. Goodenough, *Electrochem. Commun.*, 2007, **9**, 1881-1885.

6. S. W. Zhang, Y. H. Wan, Z. D. Xu, S. S. Xue, L. J. Zhang, B. Z. Zhang and C. R. Xia, *J. Mater. Chem. A*, 2020, **8**, 11553-11563.

7. J. L. Y. Sun, Y. Zeng, B. S. Amirkhiz, M. Wang, Y. Behnamian and J. Luo, *J. Mater. Chem. A*, 2015, **3**, 11048-11056.

8. Y.-F. Sun, Y.-Q. Zhang, J. Chen, J.-H. Li, Y.-T. Zhu, Y.-M. Zeng, B. S. Amirkhiz, J. Li, B. Hua and J.-L. Luo, *Nano Letters*, 2016, **16**, 5303-5309.

9. N. Zhou, Y.-M. Yin, Z. Chen, Y. Song, J. Yin, D. Zhou and Z.-F. Ma, *J. Electrochem. Soc.*, 2018, **165**, F629-F634.

10. R. Glaser, T. Zhu, H. Troiani, A. Caneiro, L. Mogni and S. A. Barnett, *J. Mater. Chem. A*, 2018, **6**, 5193-5201.

11. T. Zhu, D. E. Fowler, K. R. Poeppelmeier, M. Han and S. A. Barnett, *J. Electrochem. Soc.*, 2016, **163**, F629-F634.

12. H. Li, Y. Song, M. Xu, W. Wang, R. Ran, W. Zhou and Z. Shao, *Energy & Fuels*, 2020, **34**, 11449-11457.

13. M. X. Qin, T. Tan, K. Li, Z. M. Wang, H. Y. Yang, Z. J. Liu, M. Y. Zhou, T. K. Liu, C. H. Yang and M. Liu, *Int. J. Hydrog. Energy*, 2020, **45**, 21464-21472.

14. A. K. Sahu, A. Ghosh, A. K. Suri, P. Sengupta and K. Bhanumurthy, *Mater. Letters*, 2004, **58**, 3332-3336.

15. T. Zhu, H. E. Troiani, L. V. Mogni, M. Han and S. A. Barnett, *Joule*, 2018, **2**, 478-496.

16. S.-L. Zhang, H. Wang, M. Y. Lu, C.-X. Li, C.-J. Li and S. A. Barnett, *J. Power Sources*, 2019, **426**, 233-241.

17. S.-L. Zhang, H. Wang, M. Y. Lu, A.-P. Zhang, L. V. Mogni, Q. Liu, C.-X. Li, C.-J. Li and S.

A. Barnett, *Energy Environ. Sci.*, 2018, **11**, 1870-1879.

18. Z. Gao, V. Y. Zenou, D. Kennouche, L. Marks and S. A. Barnett, *J. Mater. Chem. A*, 2015, **3**, 9955-9964.

19. Z. Gao, D. Kennouche and S. A. Barnett, *J. Power Sources*, 2014, **260**, 259-263.

20. M. Santaya, L. Toscani, L. Baqué, H. E. Troiani and L. Mogni, *Solid State Ionics*, 2019, **342**, 115064.

21. C. Yang, Z. Yang, C. Jin, G. Xiao, F. Chen and M. Han, *Adv. Mater.*, 2012, **14**, 1439-1443.

22. S. Liu, K. T. Chuang and J.-L. Luo, *ACS Catalysis*, 2016, **6**, 760-768.

23. Y.-F. Sun, J.-H. Li, L. Cui, B. Hua, S.-H. Cui, J. Li and J.-L. Luo, *Nanoscale*, 2015, **7**, 11173-11181.

24. Y.-F. Sun, X.-W. Zhou, Y. Zeng, B. S. Amirkhiz, M.-N. Wang, L.-Z. Zhang, B. Hua, J. Li, J.-H. Li and J.-L. Luo, *J. Mater. Chem. A*, 2015, **3**, 22830-22838.

25. J.-H. Myung, D. Neagu, D. N. Miller and J. T. S. Irvine, *Nature*, 2016, **537**, 528-531.

26. D. Dong, X. Shao, X. Hu, K. Chen, K. Xie, L. Yu, Z. Ye, P. Yang, G. Parkinson and C.-Z. Li, *Int. J. Hydrogen Energy*, 2016, **41**, 19829-19835.

27. A. Leonide, V. Sonn, A. Weber and E. Ivers-Tiffee, *J. Electrochem. Soc.*, 2008, **155**, B36-B41.

28. H. Zhu, R. J. Kee, V. M. Janardhanan, O. Deutschmann and D. G. Goodwin, *J. Electrochem. Soc.*, 2005, **152**, A2427-A2440.

29. S. Dierickx, A. Weber and E. Ivers-Tiffée, *Electrochim. Acta*, 2020, **355**, 136764.

30. M. Heinzmann, A. Weber and E. Ivers-Tiffée, *J. Power Sources*, 2019, **444**, 227279.

31. S. Dierickx, T. Mundloch, A. Weber and E. Ivers-Tiffée, *J. Power Sources*, 2019, **415**, 69-

82.

32. M. Y. Lu, R. Scipioni, B.-K. Park, T. Yang, Y. A. Chart and S. A. Barnett, *Mater. Today Energy*, 2019, **14**, 100362.

33. D. A. Osinkin, N. M. Bogdanovich and A. L. Gavrilyuk, *Electrochim. Acta*, 2016, **199**, 108-115.

34. T. Ramos, K. Thydén and M. Mogensen, *ECS Transactions*, 2010, **28**, 123-139.

35. S.-L. Zhang, D. Cox, H. Yang, B.-K. Park, C.-X. Li, C.-J. Li and S. A. Barnett, *J. Mater. Chem. A*, 2019, **7**, 21447-21458.

36. M. Kilo, C. Argirusis, G. Borchardt and R. Jackson, *Phy. Chem. Chem. Phy.*, 2003, **5**, 2219-2224.

37. R. Doshi, V. L. Richards, J. D. Carter, X. Wang and M. Krumpelt, *J. Electrochem. Soc.*, 1999, **146**, 1273-1278.

38. D. Sarantaridis and A. Atkinson, *Fuel Cells*, 2007, **7**, 246-258.

39. A. Faes, A. Nakajo, A. Hessler-Wyser, D. Dubois, S. A. Brisse, Modena and J. V. herle, *J. Power Sources*, 2009, **193**, 55-64.

40. D. M. Bierschenk, E. Potter-Nelson, C. Hoel, Y. Liao, L. Marks, K. R. Poeppelmeier and S. A. Barnett, *J. Power Sources*, 2011, **196**, 3089-3094.

41. Z. Du, H. Zhao, S. Yi, Q. Xia, Y. Gong, Y. Zhang, X. Cheng, Y. Li, L. Gu and K. Świerczek, *ACS Nano*, 2016, **10**, 8660-8669.

42. J. R. Fleig, *Annu. Rev. Mater. Res.*, 2003, **33**, 361-382.

43. Z. Gao, L. V. Mogni, E. C. Miller, J. G. Railsback and S. A. Barnett, *Energy Environ. Sci.*, 2016, **9**, 1602-1644.

44. A. Nenning, L. Volgger, E. Miller, L. V. Mogni, S. A. Barnett and J. Fleig, *J. Electrochem. Soc.*, 2017, **164**, F364-F371.

45. S. J. Zhou, Y. Yang, H. Chen and Y. H. Ling, *Ceram. Int.*, 2020, **46**, 18331-18338.

46. X. Y. Meng, Y. Wang, Y. Q. Zhao, T. H. Zhang, N. Yu, X. Chen, M. Y. Miao and T. Liu, *Electrochim. Acta*, 2020, **348**, 12.

47. T. Liu, Y. Q. Zhao, X. Y. Zhang, H. Zhang, G. Jiang, W. Zhao, J. Y. Guo, F. L. Chen, M. F. Yan, Y. X. Zhang and Y. Wang, *J. Mater. Chem. A*, 2020, **8**, 582-591.

48. R. A. George, *J. Power Sources*, 2000, **86**, 134-139.

49. K. Huang and S. C. Singhal, *J. Power Sources*, 2013, **237**, 84-97.

50. T. Tsai and S. A. Barnett, *Solid State Ionics*, 1997, **98**, 191-196.

51. C. Yuan, Y. Liu, Y. Zhou, Z. Zhan and S. Wang, *Int. J. Hydrogen Energy & Fuels*, 2013, **38**, 16584-16589.

52. L. N. Shu, J. Sunarso, S. S. Hashim, J. K. Mao, W. Zhou and F. L. Liang, *Int. J. Hydrog. Energy*, 2019, **44**, 31275-31304.

53. X. J. Chen, Q. L. Liu, S. H. Chan, N. P. Brandon and K. A. Khor, *Electrochem. Commun.*, 2007, **9**, 767-772.

54. H. Kurokawa, L. Yang, C. P. Jacobson, L. C. D. Jonghe and S. J. Visco, *J. Power Sources*, 2007, **164**, 510-518.

55. X. Yang and J. T. S. Irvine, *J. Mater. Chem.*, 2008, **18**, 2349-2354.

56. G. Tsekouras, D. Neagu and J. Irvine, *Energy Environ. Sci.*, 2012, **6**, 256-266.

57. S. Liu, Q. Liu and J.-L. Luo, *J. Mater. Chem. A*, 2016, **4**, 17521-17528.

58. Y. Wang, T. Liu, M. Li, C. Xia, B. Zhou and F. Chen, *J. Mater. Chem. A*, 2016, **4**, 14163-

14169.

59. B. Hua, M. Li, Y.-F. Sun, J.-H. Li and J.-L. Luo, *ChemSusChem*, 2017, **10**, 3333-3341.

60. H. Lv, L. Lin, X. Zhang, D. Gao, Y. Song, Y. Zhou, Q. Liu, G. Wang and X. Bao, *J. Mater. Chem. A*, **7**, 11967-11975.

61. W. Wang, L. Gan, J. Lemmon, F. Chen, J. Irvine and K. Xie, *Nature Commun.*, 2019, **10**, 4727.

62. O. Kwon, K. Kim, S. Joo, H. Y. Jeong, J. Shin, J. W. Han, S. Sengodan and G. Kim, *J. Mater. Chem. A*, 2018, **6**, 15974-15953.

63. D. Papargyriou, D. N. Miller and J. T. S. Irvine, *J. Mater. Chem. A*, 2019, **7**, 15812-15822.

64. T. H. Wan, M. Saccoccio, C. Chen and F. Ciucci, *Electrochem. Acta*, 2015, **184**, 483-499.